



# Influence of the deposition pattern on the interlayer fracture toughness of FDM components

Francesco Lambiase<sup>1</sup> · Antonios G. Stamopoulos<sup>1</sup> · Francesco Pace<sup>1</sup> · Alfonso Paoletti<sup>1</sup>

Received: 28 June 2023 / Accepted: 24 August 2023 / Published online: 29 August 2023  
© The Author(s) 2023

## Abstract

The present work is aimed at studying the influence of the deposition strategy on the fracture toughness behavior of the interlayer zone of fused deposition modeling (FDM) 3D-printed parts. Double cantilever beam (DCB) specimens were produced and tested following recognized testing protocols to capture the fracture toughness behavior. The tested conditions involved linear patterns with monodirectional and alternate infill strategies. The difference in the mechanical behavior of the samples was crossed with optical microscopy observations that also enabled the precise quantification of the effective bonding area between consecutive layers. The results indicated that the deposition pattern dramatically influenced the fracture toughness behavior of these components. Monodirectional deposition strategies involved a fracture toughness within 0.75 and 2.4 kJ/m<sup>2</sup> for 0° and 90° raster angles, respectively. On the other hand, the fracture toughness of samples manufactured with alternate deposition strategies more than doubled the values mentioned above, being 2 kJ/m<sup>2</sup> and 3.9 kJ/m<sup>2</sup> for 0/90° and ±45° deposition strategies, respectively, significantly affecting the failure mode as well. These differences become even more evident if the effective bonding area between consecutive layers is considered.

**Keywords** Mechanical behavior · Fused deposition modeling · Additive manufacturing · Fracture toughness · Interlayer bonding · Interlayer adhesion

## Abbreviations

<i>a</i>	Pre-crack length
<i>a</i> <sub>0</sub>	Initial pre-crack length
<i>b</i>	Specimen width
BT	Beam theory
<i>C</i>	Ratio between the load point displacement and the applied load
DCB	Double cantilever beam
<i>E</i> <sub>11</sub>	Elastic module along the specimen direction
FDM	Fused deposition modeling
<i>G</i> <sub>IC</sub>	Critical energy release rate
<i>h</i>	Specimen overall thickness
MBT	Modified beam theory
<i>P</i>	Applied load
<i>t</i>	Distance between the loading block and the mid-plane of the first substrate
<i>δ</i>	Machine crosshead displacement

## 1 Introduction

Additive manufacturing (AM) is catching on as a new and promising technology that may produce final components or prototypes with complicated geometry while overcoming the constraints imposed by traditional fabrication methods. According to the requirements of each application, the AM techniques offer a wide range of materials and machines, excellent design freedom, and minimal fixed costs [1, 2]. Due to its proven benefits, FDM is a versatile subset of the existing AM methods for creating polymer components. To generate the finished product, layers of polymer filaments are deposited in a way to create a predetermined repetitive pattern. These filaments are heated up to a temperature at which they either become viscous or melt, at which point they are extruded from a nozzle. One of the most significant benefits of this technology is the ability to build items using a variety of engineered polymers, such as polycarbonate (PC) [3] or polyamide (PA) [4], techno-polymers such as polyetheretherketone (PEEK) [5], polyethyleneimine (PEI) [6], and polyaryletherketone (PAEK) [7], or even polymers reinforced with short or continuous fibers [8–10]. Given recent developments, FDM is scalable since it allows for

✉ Francesco Lambiase  
francesco.lambiase@univaq.it

<sup>1</sup> Department of Industrial and Information Engineering and Economics (DIIE), University of L'Aquila, Monteluco di Roio, 67100 L'Aquila, Italy

the fabrication of objects of any size, which helps to meet the criteria for a more extensive circular economy.

Despite the benefits of these techniques, a lot of work is put into identifying and improving the features of AM products connected to the processing circumstances [11, 12]. These factors mainly involve the repeatability of the deposition conditions and the minimization of defects, such as pores and voids, the lack of adequate adhesion between the deposited layers, and shrinkage and warpage related to the heat cycles involved. All these issues might result in a difference in mechanical behavior between the designed and manufactured products since they emerge at different scales, from micro to macro. As a result, various investigations explored the correlation between the deposition features of AM components' mechanical behavior [5–14]. The majority of these works focus on tensile [8], tensile and flexural [9], or even indentation [13, 14], combined non-destructive and tensile tests [10], and compressive [12] to gain a thorough understanding of how manufacturing parameters affect the damage mechanisms that are being introduced.

The raster angle, formed by the direction in which the raster is deposited and the direction in which it is being loaded, significantly impacts the mechanical behavior of FDM parts. When applied along it, the raster bears the load (raster angle of  $0^\circ$ ), and the sample exhibits mechanical behavior resembling to injection-molded components [15]. The sample shows lower strength and lower elongation at break, which implies a more brittle behavior when the load is applied transversely to the raster (raster angle of  $90^\circ$ ). This circumstance causes the bond surface between the filaments to become loaded, which worsens the related mechanical properties. As a result, these components exhibit significant anisotropy. The mechanical behavior along the building direction (z-direction) cannot be improved this way, even though planar anisotropy can be reduced by switching between layers with various orientations. This has motivated numerous researchers to use an integrative approach to examine interlayer adhesion. This field has encountered a variety of strategies:

- Analysis of the FDM parameters' effects on interlayer adhesion: this field of research is aimed at understanding how the process parameters affect adhesion and identifying potential interactions between the process parameters with the ultimate aim of identifying the ideal processing conditions that maximize the interlayer bond;
- Post-processes: this field focuses on figuring out how to modify the build component to increase the interlayer bonding (for example, by encouraging intermolecular diffusion or by raising the crystallinity in semicrystalline polymers);
- Mechanical characterization: by recording the actual behavior of the interlayer bond, this area is aimed at

choosing the best characterization tests. This would enable forecasting a component's mechanical characteristics for use in structural design.

There has been a significant advancement in the third field of inquiry. The testing procedures, including those in the area of characterizing the interlaminar fracture toughness in various modes, were summarized by Gao et al. [15]. To calculate the  $J$  integral, Aliheidari et al. [16] investigated mode I fracture toughness tests performed on ABS specimens produced using FDM. Both reinforced and pure ABS specimens underwent a fracture toughness assessment by Young et al. [17].

The interlayer toughness of pure polyamide (PA12) and polyamide reinforced with short fibers was evaluated by Fonseca et al. [18]. Double cantilever beam (DCB) specimen was utilized by Barile et al. [19] to assess the mode I fracture toughness of PLA samples. Khudiakova et al. [20] examined the difference in the mode I fracture toughness between PLA and carbon-reinforced PLA.

To examine mode I fracture toughness properties of PA 2200, Marsavina et al. [21] analyzed two testing standards established for bulk or composite materials. Santos et al. [22] used ISO and ASTM testing standards to perform mode I and mode II fracture toughness tests on 3D-printed polyamide/continuous carbon fiber-reinforced specimens. A simple tensile specimen with a notch is put under cyclic strain using the SENB testing method, which was very recently established [23].

However, this situation has certain restrictions, including unstable crack propagation and high plasticity in the crack's vicinity. Other times, static mode I and 3-point bending experiments were carried out by Fazlay Rabbi and Chalivendra [24] to assess the fracture toughness under mode I and mixed mode crack opening at the interface between PLA and nylon asymmetric specimens. In this instance, the pre-crack was first introduced using a polyimide tape.

Due to the similarities concerning the mechanical behavior between composite materials and additively generated components, testing standards for composite materials are used in most studies to assess the fracture toughness of additively manufactured parts. Additionally, the pre-crack was often accomplished by inserting a film in the midplane to fabricate the specimen [17–22]. The film only tenuously clings to the substrate, allowing further layers of deposition. This process required interrupting the deposition to install the film, which also calls for careful handling.

As a result, the release film may cause some problems since the deposition process is interrupted, and a more extended period passes before moving on to the following layer. When installing the subsequent layer, this requires a faster cooling of the substrate. As a result, the substrate cools down more quickly than it would under normal deposition

circumstances. This results in a change in the heat cycle that could potentially lead to a deviation in the interlayer mechanical characteristics [25, 26]. Additionally, the placement of the release film requires the presence of an operator during the entire process, which is risky for human mistakes and becomes even more difficult when using high-temperature polymers. A new sample configuration involving nested spacers was proposed in [27] to overcome such limitations. This sample configuration enabled the identification of the interlayer fracture toughness with great accuracy without coming across the abovementioned limitations.

In the present study, the influence of the deposition strategy on the fracture toughness of FDM samples was investigated using double cantilever beam (DCB) specimens. Optical microscopy of the fractured surfaces was performed to understand better how the deposition strategy influences the adhesion between consecutive layers.

## 2 Materials and methods

### 2.1 Geometry of the specimens

The DCB specimen of the present work, whose basic geometry was defined following ASTM D5528 standard [28], was the one that was also used in past works [27] incorporating nested spacers in a slot. A scheme of the DCB sample is reported in Fig. 1. Here, the subsequent layers are depicted with different colors to identify the printing strategy better. This slot was created by imposing the removal of two layers of filaments, creating a pre-crack of initial length  $\alpha_0$ .

Therefore, the pre-crack zone had an initial thickness of 2 filament layers. A crucial component of the test appropriateness is determined by the samples' geometrical features, such as their overall thickness, the distance between the two substrates' midplanes and the loading

blocks, and their pre-crack length. The dimensions of the samples were identified to comply with Equations 1, 2, and 3, which are related to the distance between the loading block and the midplane of the first half of the specimen ( $t$ ), the minimum overall specimen thickness ( $h$ ), and the pre-crack length ( $\alpha_0$ ).

$$t \leq \frac{h}{4} + 0.01 \sqrt{\frac{0.0434h^3 + E_{11}}{G_{Ic}}} + a^2 \tag{1}$$

$$h \geq 8.28 \sqrt[3]{\frac{G_{Ic} a_0^2}{E_{11}}} \tag{2}$$

$$\alpha_0 \leq 0.042 \sqrt{\frac{h^3 E_{11}}{G_{Ic}}} \tag{3}$$

where  $E_{11}$  is the elastic module along the x-direction,  $G_{Ic}$  is the expected critical energy release rate,  $\alpha$  is the pre-crack length, and  $\alpha_0$  is the pre-crack length starting from the load line axis as seen in Fig. 2. Tensile tests were conducted using a universal testing machine model Criterion 43.50 by MTS, following the ASTM D638 standards, under room conditions, and at a crosshead speed of 1 mm/min to determine longitudinal Young's modulus  $E_{11}$  of the PLA of the identical filaments. The observed modulus  $E$  was found to vary between 2.8 GPa and 3.3 GPa in the various filament orientations tested.

As a result, the minimum overall thickness of the samples was established to be between 4.5 and 7.5 mm, also dependent on the factors above and the crack length. As shown in Fig. 1, the characteristic dimensions of the samples were determined by taking into account the mechanical behavior of polylactic acid (PLA) and compliance with the recommendations of the relevant testing standard [28].

**Fig. 1** Relative direction between filaments and applied load

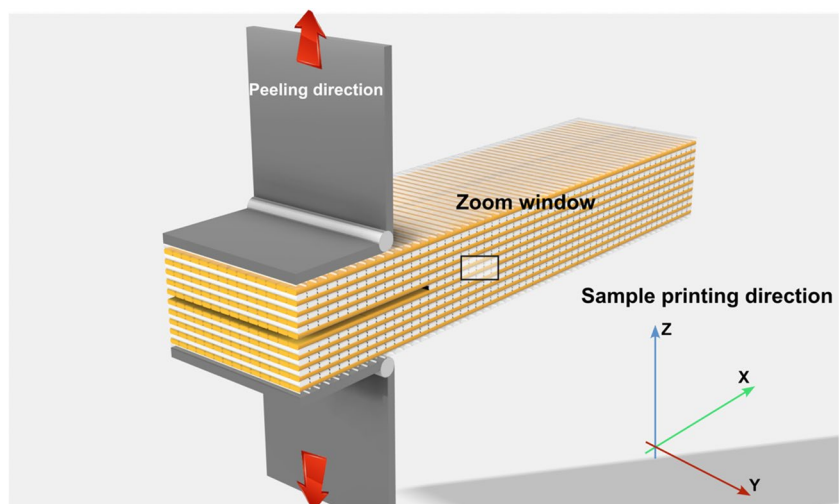
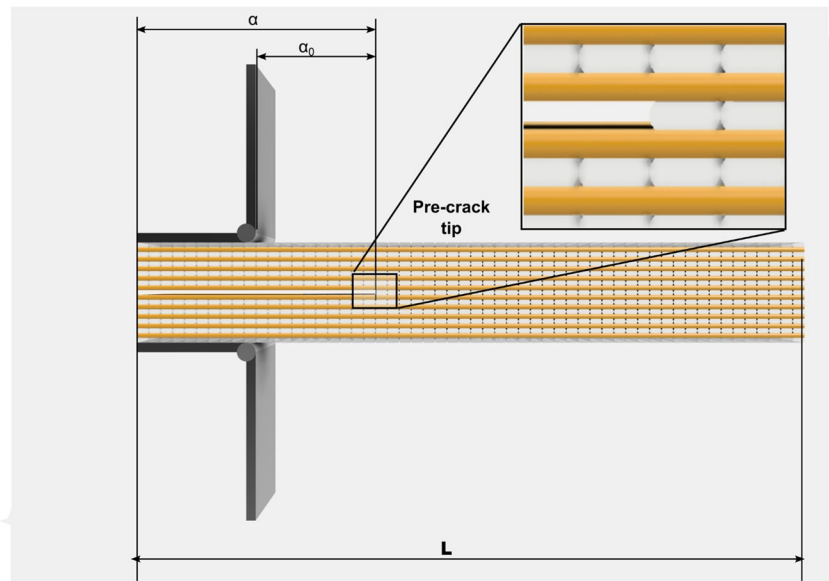


**Fig. 2** Main dimensions of the samples used in the experimentations



The characteristic dimensions of the samples, which are schematically depicted in Fig. 2. The typical specimen is composed of a total length ( $L$ ) of 125 mm and a width of 25 mm respectively. The precrack length  $\alpha$  was 55 mm while the distance between the load line and the initial crack tip  $\alpha_0$  was 30 mm.

## 2.2 Sample material and printing

0.2 mm thick layers were adopted (corresponding to 50% of the adopted nozzle diameter  $d=0.4$  mm). The load line was designed perpendicular to the printing plane in all examples.

Different infill strategies were adopted, monodirectional and alternating strategies, as schematized in Fig. 3. The multiplier for extrusion was set to 100%. Any exterior shell was used during the specimen manufacturing process to create a homogeneous sample. For each deposition strategy, five repetitions were performed.

## 2.3 Specimen preparation and characterization process

A pair of steel piano hinges were adhesively bonded at the part of each specimen that incorporated the precrack to provide the load necessary to open the crack, as

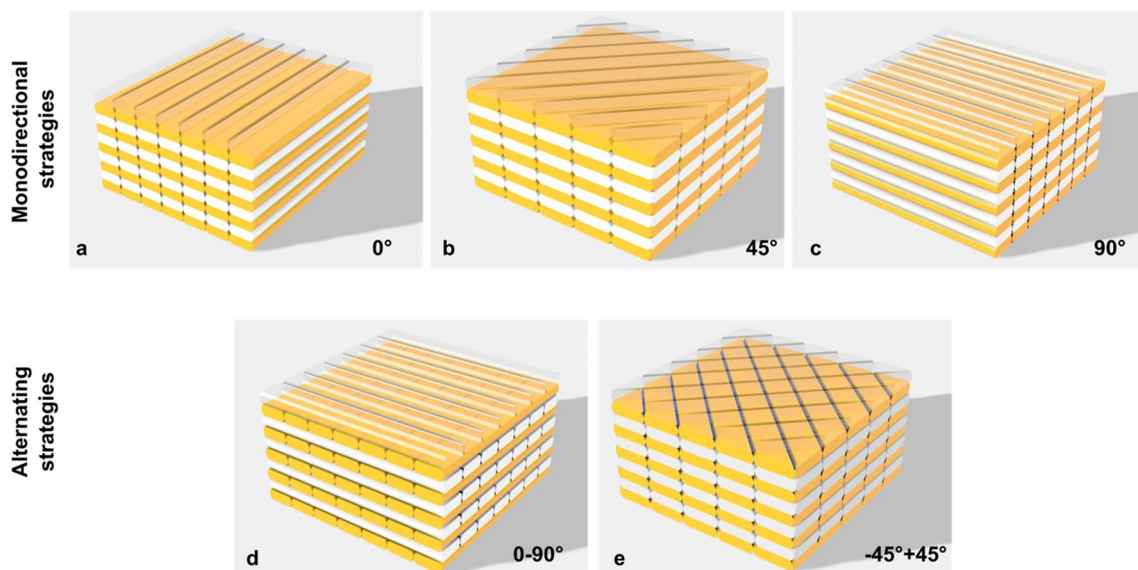


**Fig. 3** Schematic of the deposition strategy used to manufacture the specimens

shown in Fig. 1. Before the application of the adhesive, a neutralizing cleaning spray was applied to prevent the presence of contaminants that could reduce the adhesion quality. This ensured a proper adhesion between the piano hinges and the sample surface. Next, a rubber-based primer agent with P400 chloric was used to pre-treat the surfaces. A constant-dosage pistol with a mixing nozzle was used to apply a structural bio-composed methacrylic Easy-Mix PE-PP 45 bi-component adhesive consistently. Both treatment and adhesive products were provided by WEICON GmbH & Co. (Munich, Germany). All the specimens were exposed to constant temperature and normal ambient conditions for roughly 24 hours to ensure the proper solidification of the adhesive agent following the indications of the DIN EN 1465 [29] standard.

An MTS Universal Testing Machine with a 50 kN applied force capacity, model C43.50, was used for the fracture toughness testing campaign. One millimeter per minute (mm/min) was chosen as the crosshead speed because it is the lowest value suggested by the related standard [28]. A 200x-capable Dino-Lite AM2111 traveling optical microscope installed on a mechanism with a movable base was used to monitor the fracture tip, as shown in Fig. 4. White paint was applied to the specimen's side surface, as well as tick marks in every 5 mm each of them, to determine the position of the crack front more precisely.

According to the testing standard, the procedure was divided into two distinct phases. The first phase is aimed at clearing the crack front and precisely identifying the crack tip position. During this phase, the specimen was loaded until a crack opening and extension was developed between the first 3 and 5 mm; then, the specimen was completely unloaded at a crosshead speed of 8 mm per minute. This step is essential for completing the test because it enables clearing the crack front from any potential geometrical flaws brought on by the 3D

printing process. Besides, it allowed the clear identification of the crack path.

During the second phase (once the crack tip is identified), a steady crosshead displacement of 1 mm/min was used to open and spread the crack. Throughout this procedure, the load applied by the testing machine and the corresponding crosshead displacement were correlated with the crack tip for every 5 mm of extension.

The VIS point technique was used to specify the fracture starting features and, as a result, the critical energy release rate. This approach records the fracture motion's start, as shown in Fig. 5a, which depicts a typical force-crosshead displacement curve. The energy needed to spread a crack over a unit surface area is represented by the mode I strain energy release rate. The DCB test for an elastic linear construction is based on the change in compliance,  $C$ , which is determined by Equation 4:

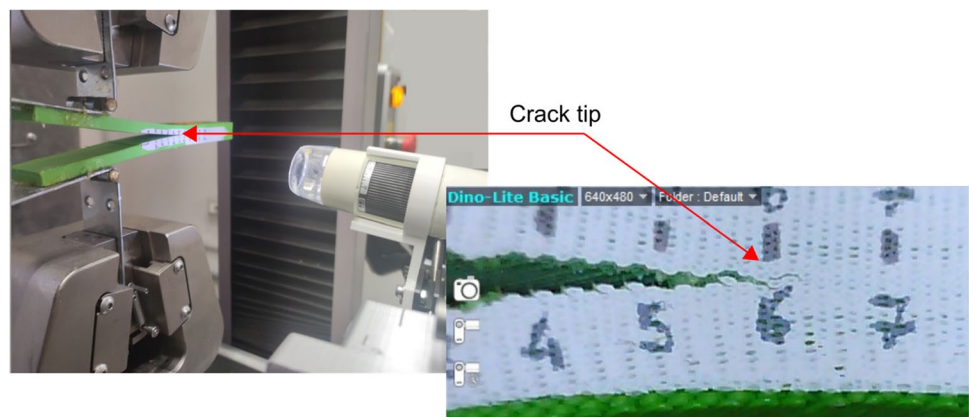
$$C = \frac{\delta}{P} \quad (4)$$

The loss of stored energy caused by the crack spreading from a value of  $a$  to  $a + \alpha$  causes a change to the compliance. The beam theory assumes that the adherents are clamped at the crack tip and that there is little spinning in this area for calculating the compliance. As a result, using the Irwin-Kies formula [30], which is given by Equation 5, it is possible to determine the strain energy release rate  $G_I$ :

$$G_I = \frac{P^2}{2b} \frac{\partial C}{\partial a} \quad (5)$$

$P$  stands for applied load and denotes machine crosshead displacement,  $b$  for specimen breadth, and the crack extension corresponds to applied load  $P$  and crosshead displacement. Thus, based on the Young modulus  $E$  (in this case equal to  $E_{11}$ ), and using Equations 6 and the Euler-Bernoulli, it is possible to determine the compliance  $C$ , displacement  $\delta$ , and moment of inertia  $I$ .

**Fig. 4** Picture of the adopted equipment during the execution of the mode I fracture toughness tests (testing machine, piano hinges, and the traveling microscope device)



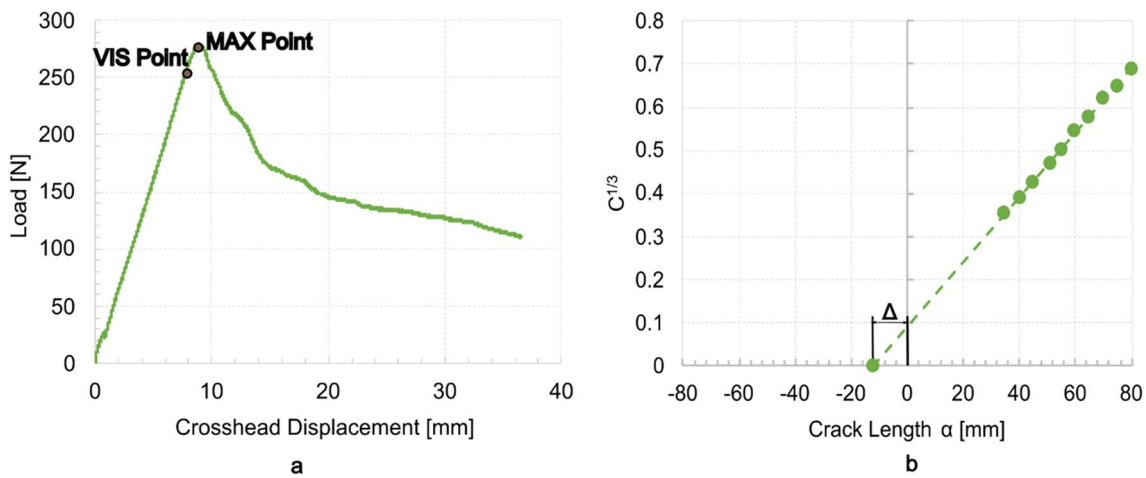


**Fig. 5** Typical load-crosshead displacement curve obtained by the execution of one of the tests (a) and defining the  $\Delta$  factor for calculating the energy release rate using the modified beam theory (b)

$$C = \frac{8a^3}{Ebh^3} \delta = \frac{2Pa^3}{3EI} I = \frac{bh^3}{12} \tag{6}$$

$$G_I = \frac{3P\delta}{2b(\alpha + |\Delta|)} \tag{8}$$

Thus, the strain release energy rate  $G_I$  is determined by Equation 7:

$$G_I = \frac{3P\delta}{2ba} \tag{7}$$

The parameter  $\Delta$  denotes the intercept of the linear regression curve between the crack length and the cube root of  $C$ , as shown in Fig. 5b.

### 3 Results

#### 3.1 Mode I fracture toughness characteristics

The same reasoning suggests that the parameters of Equation 5 could be used to remedy any possible incorrect fracture front detection. According to Equation 8, the modified beam theory approach was utilized to determine the energy release rate  $G_I$ :

The applied load-crosshead displacement curves for each type of specimen are reported in Fig. 6a with different colors for each

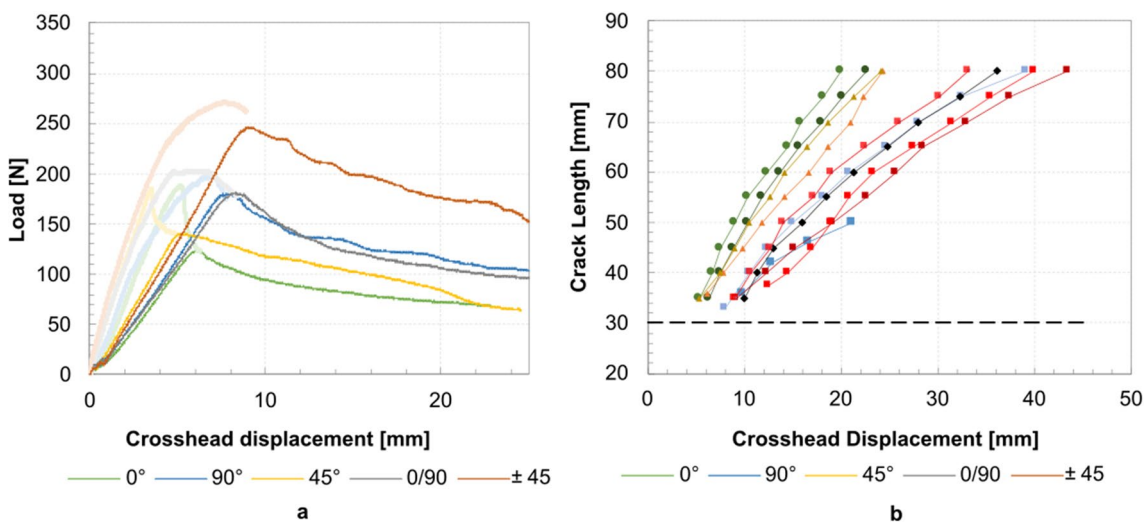


**Fig. 6** The load-crosshead displacement curves of representative specimens of each category (a) and the crack length-crosshead displacement ratio obtained by the experimental campaign (b)

specimen category. The blur curves represent the load-crosshead displacement during the first phase of the execution of the test.

The configuration of pure longitudinal filaments in the crack interface ( $0^\circ$ ) required less load than the rest of the configurations. At the same time, the  $\pm 45^\circ$  gained the highest values of applied load and related crosshead displacement. The pure  $90^\circ$  and  $0/90^\circ$  configurations show similar load-crosshead displacement curves. Nevertheless, some interesting aspects are presented in the corresponding crack length-crosshead displacement curves of Fig. 6b.

The energy release rate  $G_I$  was computed using the equations of the simple and modified beam theories described in Section 2. Figure 7 shows the average values of the critical energy release rate and the crack propagation for the deposited strategies.

The results reported in Fig. 7 indicate a strong influence of the deposition strategy on the  $G_{Ic}$  and  $G_{Iprop}$ . Monodirectional strategies involving filaments parallel to the crack propagation path ( $0^\circ$ ) involved average values of 0.74 and 0.71  $\text{kJ/m}^2$  for the  $G_{Ic}$  and the  $G_{Iprop}$ , respectively. These samples were characterized by the lowest values of  $G_{Ic}$  and  $G_{Iprop}$  as compared to the other deposition strategies. The deposition strategy that enabled the highest values of fracture toughness was  $\pm 45^\circ$ . These samples showed a  $G_{Ic}$ , which was 3.9  $\text{kJ/m}^2$ , almost 4.4 times the values recorded for  $0^\circ$  samples.  $\pm 45^\circ$  samples were also characterized by higher standard deviation that was presumably attributed to the failure mode also captured by the optical microscopy. For the monodirectional  $45^\circ$  strategy, the average values of  $G_{Ic}$  and  $G_{Iprop}$  showed high standard deviation. Indicatively, the values of  $G_{Ic}$  ranged between 0.94 and 2.10  $\text{kJ/m}^2$ , while the  $G_{Iprop}$  varied between 1.03 and 2.45  $\text{kJ/m}^2$ , respectively.

Monodirectional  $90^\circ$  and alternate samples  $0/90^\circ$  showed similar fracture toughness values for crack initiation and propagation. These two categories shared similar behavior

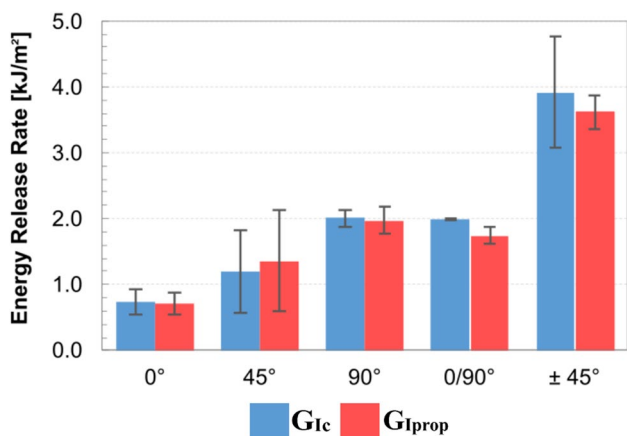


Fig. 7 The average values of the critical ( $G_{Ic}$ ) and the propagation release rate ( $G_{Iprop}$ ) obtained by the testing campaign

regarding applied load and crosshead displacement, even though the deposition strategy and the related bonding between the adjacent filament layers differed. It should also be noted that in these two cases, the standard deviation was the minimum compared to all the other specimen series indicating a more reliable behavior.

The  $R$ -curves of all the conducted tests are reported in Fig. 8 and are clustered into five groups that refer to the printing adopted strategies. In the graph, the dashed line represents the initial pre-crack length while the various specimen categories are grouped using a basic color and point shape for each one of them. For instance, the  $\pm 45^\circ$  specimens'  $R$ -curves are presented with varying tonalities of red colour and rectangular point shape. Individually, the various specimen categories showed different energy dissipation behavior. A region of increased plasticity characterized the  $\pm 45^\circ$  specimens at the beginning of the pre-crack that increased the energy demand for crack development. Consecutively, after almost 10 mm of crack propagation, the energy required stabilized at lower values, indicating a stable crack propagation between the  $+45^\circ$  and  $-45^\circ$  filament layers. However, some specimens required higher energy for crack propagation, starting from a crack length between 55 and 60 mm. A similar phenomenon was observed in [18], which attributed the increase in the fracture toughness energy to the behavior of PLA. The increased deviation between the energy release values obtained by the same specimen category should also be noted.

A similar behavior, with less intensity, was observed on  $90^\circ$  samples where the corresponding  $R$ -curves demonstrated less deviation. Since the filaments are oriented perpendicular to the crack propagation direction in these samples, the crack was progressively developed in each filament line and showed increased energy values compared to  $0^\circ$  samples. Compared to them, the  $0/90^\circ$  sample  $R$ -curve may be divided into two distinct regions: the one where the crack develops (pre-crack), and the stable crack propagates, leading to lower energy release values. Even though the  $90^\circ$

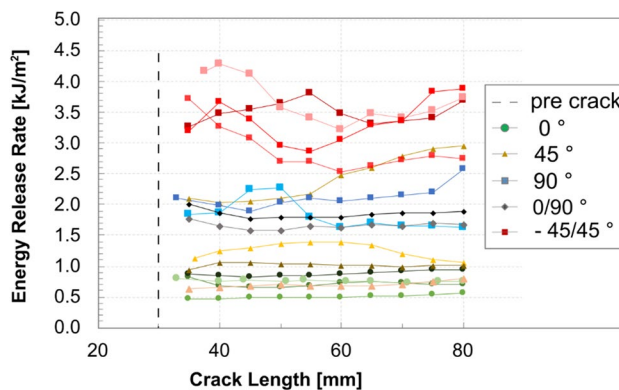


Fig. 8 The  $R$ -curves for the mode I fracture toughness test specimens

and 0/90° samples derived similar average values of  $G_{Ic}$ . monodirectional 90° and alternate 0/90° samples exhibited different energy dissipation behavior. This can be attributed to the effective bonded area in the specimens midplane. Finally, 0° samples showed the most stable crack propagation after the first 5 mm of the crack front extension. The lowest values of the energy requirements for crack propagation characterized these samples.

### 3.2 Optical microscopy

During the mode I test, PLA was prone to change the plane of the crack propagation; thus, optical microscopy was conducted to analyze the fractured surfaces. In Fig. 9, the typical fractured surfaces of the various samples are depicted as obtained by the microscopy analysis utilizing a LEICA M205A stereoscope. In the present work, the raster angle substantially affected the crack propagation within the additively manufactured PLA layers.

The specimens with a deposition angle of 0°, shown in Fig. 9a, were characterized by the most stable crack propagation without layers exfoliation. This stable crack initiation and propagation confirm the results of the  $R$ -curves. The samples with a 90° deposition strategy, shown in Fig. 9b, and alternating strategies with 0/90° deposition, depicted in Fig. 9c, also showed stable crack propagation. Nevertheless, substantial differences were found in the load-displacement curves of 0° and 90° as shown in Fig. 10. The curve of 90° samples showed a large number of load drops related to the sudden propagation of the crack from a filament to the adjacent one in the same plane. This phenomenon did not occur in the 0° samples. In 90° samples, the crack front reached the next filament after the sudden load drop, which developed in correspondence with the region with an absence of material. Transverse filament strategies behaved as a barrier that

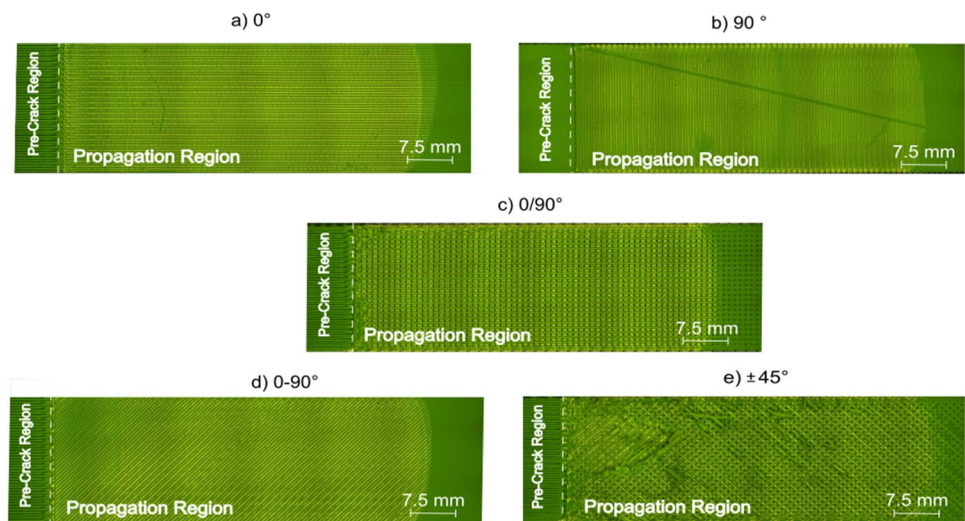
prevented the continuous propagation of the crack. Under these conditions, higher energy was required to initiate crack when the crack jumped from one filament to the next. In these cases, a constant load was required to propagate the crack front. As reported in Fig. 10, the load-crosshead displacement in the case of the 90° samples was characterized by regions of load drops due to the transition from one filament to the next one (adhesion between adjacent filaments) that led to sudden crack propagation.

The samples with strategies involving 45° and the ±45° showed completely different fracture toughness behavior. Some 45° samples showed a phenomenon similar to the kissing bond [31] after the crack initiation. Indeed, even though the adjacent filaments were in contact, they did not adhere properly, leading to locally unstable crack propagation. Besides, the ±45° specimens showed large layer pull-out regions, indicating a potential mixed-mode crack opening.

Finally, it should be noted that in some rare cases of the samples incorporating 90° deposited filaments, the crack propagation followed an out-of-plane path transverse to the longitudinal sample direction, as shown in Fig. 11. This was due to the reduced fracture toughness in that direction, compared to the in-plane fracture toughness, and the relatively low bending stiffness of the specimen arm. When this phenomenon occurred, the sample was not considered for calculating the energy release rate.

Optical microscopy analysis was also performed to determine the effective adhesion area between consecutive layers. During the FFF process, gaps are produced between consecutive filaments; while the fracture toughness computation refers to a complete adhesion between the layer surface. Figure 12 shows the adhesion surfaces of samples made under different deposition conditions. For each one, the effective area was determined by focusing on the fractured surfaces and specifying the effective filament

**Fig. 9** The characteristics of the fractured zones as observed with the optical microscope for the various specimen categories





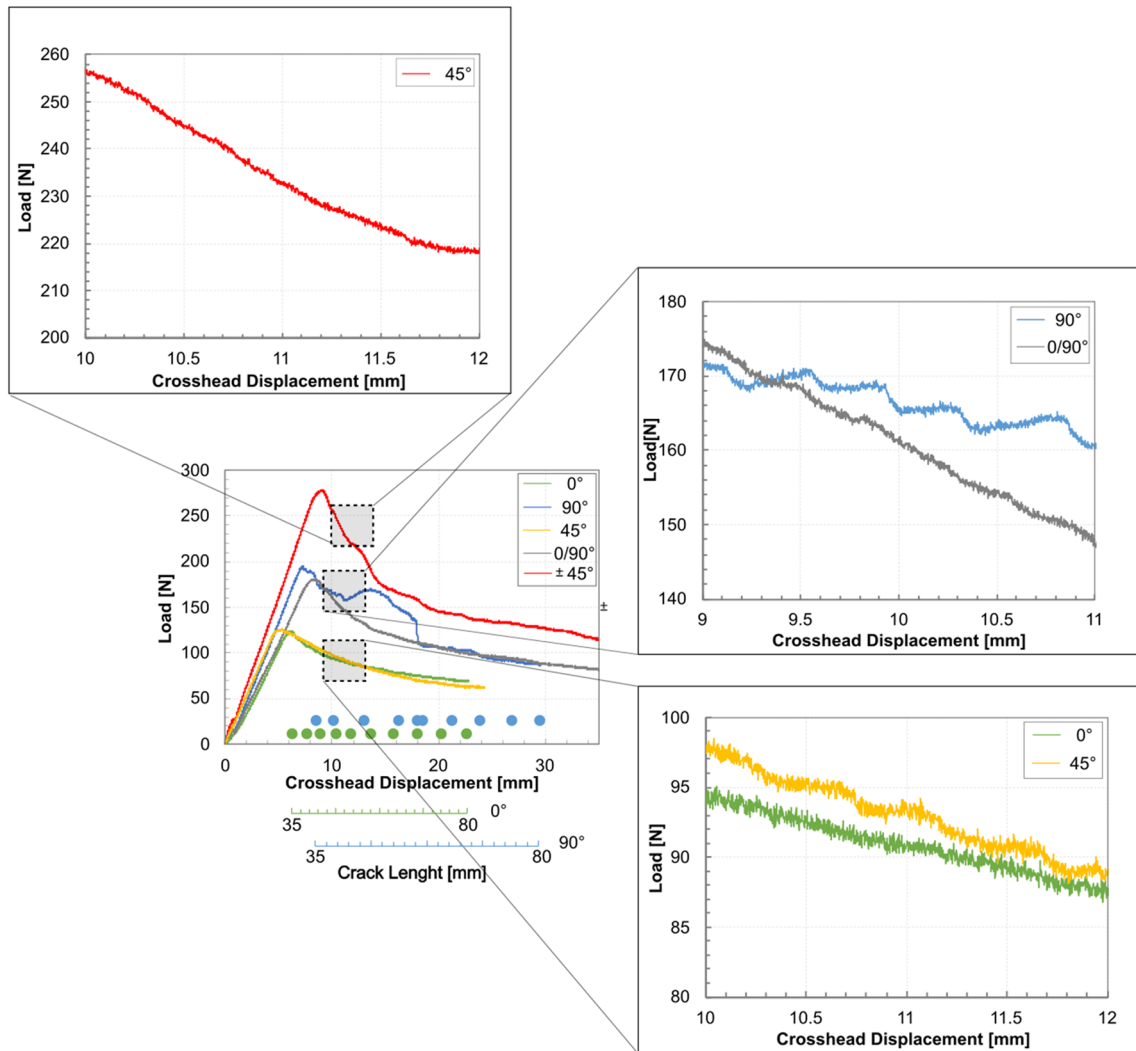
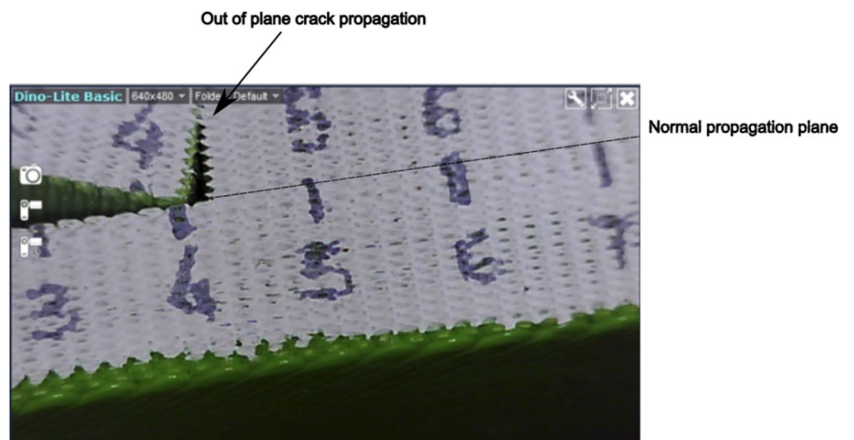
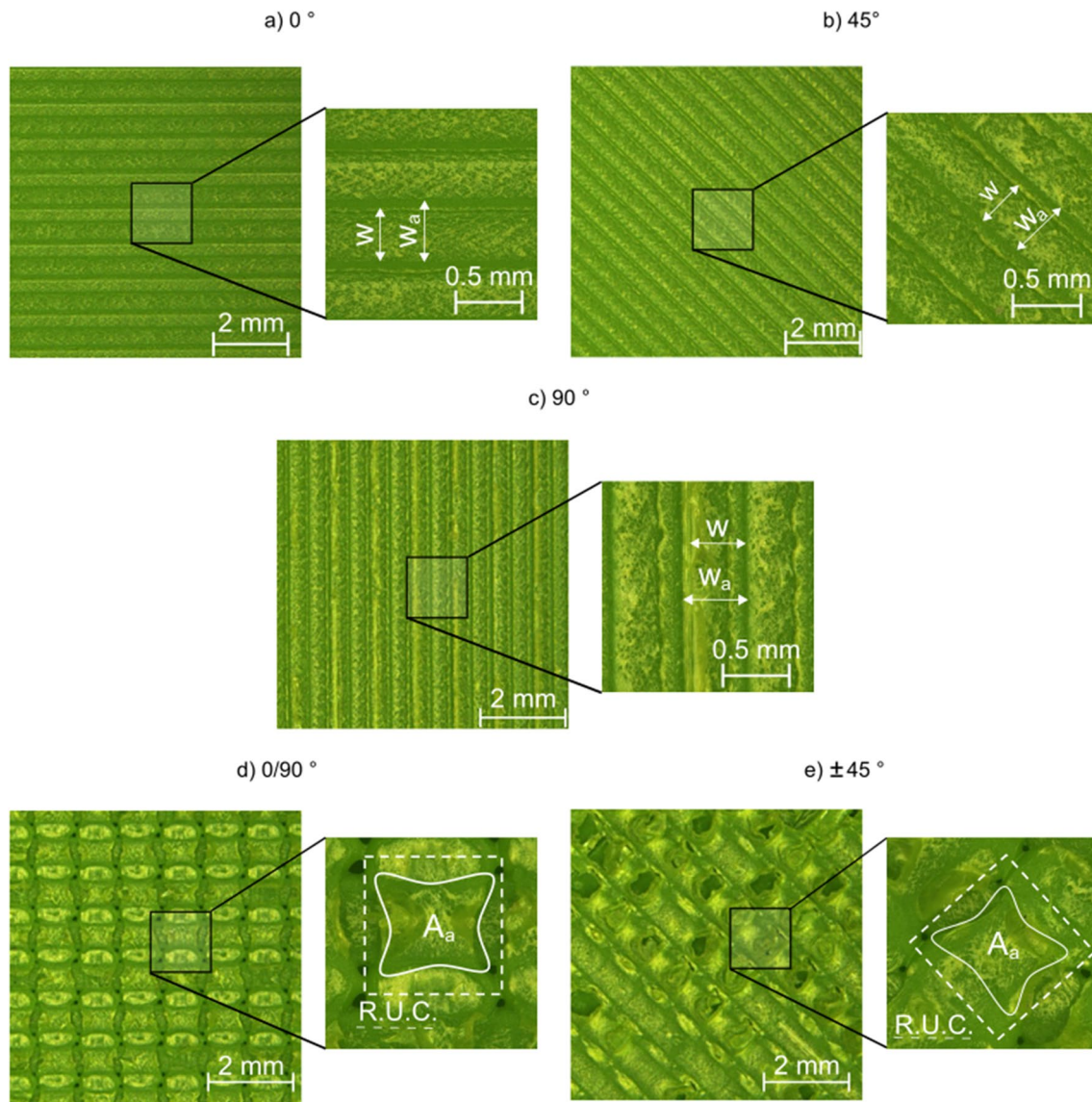


Fig. 10 Characteristics of the load-crosshead displacement curves referring to the crack propagation of the various specimens

Fig. 11 Out-of-plane crack propagation as observed by the traveling microscope for the case of a 90° sample





**Fig. 12** Macrographs of the adhesion surfaces from samples produced under different deposition conditions

bonding area. For monidirectional deposition strategies, where all the layers were deposited along the same direction, the determination of the effective adhesion area was relatively simple. Indeed, it demanded the identification of the width of contact  $w_a$ . On the other hand, for alternated deposition strategies (i.e.,  $0^\circ/90^\circ$  and  $\pm 45^\circ$ ) the adhesion area  $A_a$  required the reconstruction of the contact region and the measurement of the area for creating the elementary representative unit cell (RUC) as indicated in Fig. 12d and Fig. 12e, respectively. To this end, the open-source software ImageJ was used.

After determining the effective bonding area, the energy release rate attributed to the effective bonding area was calculated by normalizing the geometrical parameters of

Equation 8. Therefore, for the sample made with monidirectional deposited filaments, the effective critical energy release rate was calculated as follows:

$$G_{I_{eff}} = \frac{G_I}{n} \quad (9)$$

where  $n$  is the contact coefficient that may be calculated as follows:

$$n = \frac{w_e}{w_a} \text{ (unidirectional filaments)} \quad (10)$$

$$n = \frac{A_e}{A_a} \text{ (alternating filaments)} \quad (11)$$

In Equation 11,  $A_e$  represents the area of the unit cell RUC. Consequently, for the case of alternative deposition strategies, this coefficient may be calculated by the ratio of the actual bonding surface and the theoretical one, as seen in Fig. 12d, e, respectively. The average values of the contact coefficient calculated using optical microscopy are reported in Table 1.

As can be inferred, alternating strategies showed a contact coefficient of  $n=43\pm 2\%$ , much lower than monodirectional strategies of  $n=70\pm 1.5\%$ . However, alternating strategies showed an average  $G_{IC}$  of 3 kJ/m<sup>2</sup>, while monodirectional strategies showed an average  $G_{IC}$  of 1.3 kJ/m<sup>2</sup>. In addition, the lowest value of  $G_{IC}$  for alternating strategies (corresponding to 0/90° deposition) was 2.01 kJ/m<sup>2</sup>, which correspondent to almost three times that observed for the minimum value of  $G_{IC}$  for monodirectional deposition (corresponding to 0° deposition) of 0.74 kJ/m<sup>2</sup>.

## 4 Discussion

The results indicate the raster angle's strong influence on the fracture toughness of additively manufactured components. This difference is depicted in the graphs of the energy release rate required for crack initiation and propagation. The fracture toughness increases in the case of monodirectional deposition strategies when the filaments are deposited perpendicularly to the crack propagation direction. Compared to monodirectional deposition strategies, the alternating deposition strategies achieved higher fracture toughness. More precisely, the  $\pm 45^\circ$  raster angle in the specimens' interface required the highest energy levels.

Since gaps between the filaments characterize the fused filament fabricated samples, there was the necessity to attribute the calculated energy to the effective contact zones that develop a bond between the layers. The effective adhesion portion was calculated using optical microscopy measurements and was found to be similar to the case of monodirectional deposition strategies. On the other hand, alternating deposition strategies showed an effective adhesion area (43%) much lower than monodirectional strategies (70%).

**Table 1** The components for calculating the effective energy release rate

Raster angle (degrees)	Contact coefficient $n$	Standard deviation	$G_{IC}$ (kJ/m <sup>2</sup> )	$G_{ICeff}$ (kJ/m <sup>2</sup> )
0	71.4 %	1.9%	0.74	1.04
90	68.6 %	4.0%	2.01	2.93
0/90	40.8 %	2.3%	1.99	4.88
45	69.8 %	3.3%	1.20	1.72
$\pm 45$	44.7 %	2.4%	3.92	8.76

Even though such lowered adhesion area, the alternating deposition strategies demonstrated higher energy release rate values and appeared to be the optimal solution when high fracture toughness values are required.

The difference regarding the fracture toughness of the PLA samples is also reflected in the fractured surfaces and, consequently, in the  $R$ -curves. The energy dissipation was highly different as the crack propagated in the various samples' interfaces that incorporated different raster angles. The AM DCB samples utilized in past works were susceptible to potential layer pull-out. For instance, Fonseca et al. [18] identified a significant layer pull-out between  $\pm 45^\circ$  deposited PA12 or even PA12 reinforced with short carbon fibers, creating irregular patterns to the corresponding  $R$ -curves. The same phenomenon was observed by Khudiakova et al. [20] in the case of unidirectionally deposited PLA and carbon fiber-reinforced PLA, respectively. In the present work, the  $G_I$  values of the 90° angle were higher than the 0°, presumably due to the increased plasticity created by the filaments transverse to the crack extension. In addition, significant filament pull-out was observed in the case of the  $\pm 45^\circ$  specimens, which complies with the observations of the past works [19]. Even though the phenomenon of the change of the crack propagation interface is common to the works that deal with the fracture toughness of polylactic acid, the increased filament pull-out led to higher energy levels required for opening and extending the crack. Occasionally and in some rare cases in the 45° samples, a zone of unstable crack propagation was observed. This particular zone was characterized by a phenomenon similar to the kissing bonding of the composite structures where there is contact without a complete adhesion between the layers.

## 5 Conclusions

The influence of the deposition strategy adopted during Material Extrusion on the fracture toughness was investigated. An experimental campaign using polylactide acid was carried out. The tests involved double cantilever beam (DCB) specimens designed in compliance with ASTM D5568 standards. Different deposition strategies were applied, including monodirectional (0°, 45°, and 90°) and alternate deposition strategies (0°/90° and  $\pm 45^\circ$ ). The adhesion areas were also investigated to compute the effective critical energy release rate. This was achieved by considering that only a portion of the layer is effectively in contact with the overlying and underlying layers. The main conclusions from this study are as follows:

- The monodirectional deposition strategy suffers from great sensitivity from the loading direction. Indeed, when the filaments are deposited perpendicularly to the crack

front extension, the samples show higher fracture toughness values (average of 2.0 kJ/m<sup>2</sup>) compared to those having all the filaments oriented longitudinally (average of 0.74 kJ/m<sup>2</sup>).

- Alternated deposition strategy led to samples with higher fracture toughness, whose values ranged between 2 kJ/m<sup>2</sup> (for 0°/90°) and 3.9 kJ/m<sup>2</sup> (±45°). Also, in this case, the higher fracture toughness was recorded when no filament was arranged along the crack propagation path.
- ±45°-oriented filaments demonstrated the highest energy release rate values overall, showing also a highly irregular fractured zone with increased filament layers pulled out during the crack propagation.
- Even though the polylactic acid is prone to layer pull-out, in the case of the monodirectional deposition strategy, the phenomenon was not present, and the crack propagation was stable.
- The orientation of the filaments in the interface has a predominant role in the fracture toughness characteristics of the structure compared to the total effective bonding area of the filaments. Even after the normalization of the energy release rate, the differences between the alternate and continuous deposited filaments were found to be even more evident.

**Author contribution** FL and AP: supervision; FL, AP, and AS: conceptualization and methodology; FP: data curation; FL, AS, AP, and FP: writing—original draft—and writing.

**Funding** Open access funding provided by Università degli Studi dell'Aquila within the CRUI-CARE Agreement.

**Data availability** The data supporting this study's findings are available from the corresponding author, Francesco Lambiase, upon reasonable request.

## Declarations

**Conflict of interest** The authors declare no competing interests.

**Open Access** This article is licensed under a Creative Commons Attribution 4.0 International License, which permits use, sharing, adaptation, distribution and reproduction in any medium or format, as long as you give appropriate credit to the original author(s) and the source, provide a link to the Creative Commons licence, and indicate if changes were made. The images or other third party material in this article are included in the article's Creative Commons licence, unless indicated otherwise in a credit line to the material. If material is not included in the article's Creative Commons licence and your intended use is not permitted by statutory regulation or exceeds the permitted use, you will need to obtain permission directly from the copyright holder. To view a copy of this licence, visit <http://creativecommons.org/licenses/by/4.0/>.

## References

1. Durão LFC, Christ A, Anderl R, Schützer A, Zancul E (2016) Distributed manufacturing of spare parts based on additive manufacturing: use cases and technical aspects. *Procedia CIRP* 57:704–709
2. Nazir A, Gokcekaya O, Billah KMM, Ertugrul O, Jiang J, Sun J, Hussain J (2023) Multi-material additive manufacturing: a systematic review of design, properties, applications, challenges, and 3D Printing of materials and cellular metamaterials. *Mater Des* 226:111661
3. Arai T, Kaqaji M (2021) Thermal performance and flow characteristics in additive manufactured polycarbonate pulsating heat pipes with Novec 7000. *Appl Therm Eng* 197:117273
4. Arunkumar N, Sathishkumar N, Sanmugapriya SS, Selvam R (2021) Study on PLA and PA thermoplastic polymers reinforced with carbon additives by 3D printing process. *Mater. Today: Proc.* 46:8871–8879
5. Liu X, Shan Z, Liu J, Xia H, Ao X, Zou A, Wu S (2022) Mechanical and electrical properties of additive manufactured high-performance continuous glass fiber reinforced PEEK composites. *Compos Part B* 247:110292
6. Abderrafai Y, Diouf-Lewis A, Sosa-Rey F, Farahani RD, Piccirelli N, Lévesque M, Therriault D (2023) Additive manufacturing and characterization of high temperature thermoplastic blends for potential aerospace applications. *Compos Sci Technol* 231:109839
7. Yi N, Davies R, Chaplin A, McCutcheon P, Ghita O (2021) Slow and fast crystallising poly aryl ether ketones (PAEKs) in 3D printing: crystallisation kinetics, morphology, and mechanical properties. *Addit. Manuf.* 39:101843
8. Hamat S, Ishak RM, Sapuan SM, Yidris N, Hussin MS, Abd Manan SM (2023) Influence of filament fabrication parameter on tensile strength and filament size of 3D printing PLA-3D850. *Mater. Today: Proc.* 74(3):457–461
9. Bardiya S, Jerald J, Satheeskumar V (2021) The impact of process parameters on the tensile strength, flexural strength and the manufacturing time of fused filament fabricated (FFF) parts. *Mater. Today: Proc.* 39(4):1362–1366
10. Glinz J, Pace F, Maurer J, Holzleitner M, Eckl M, Vopalensky M, Kumpova I, Kastner J, Stamopoulos A, Senck S (2023) Influence of continuous fiber reinforcement on tensile properties in fused filament fabricated specimens. *AIAA SCITECH 2023 Forum*.
11. Yang Y, Gong Y, Qu S, Xie H, Cai M, Xu M (2020) Densification, mechanical behaviors, and machining characteristics of 316L stainless steel in hybrid additive/subtractive manufacturing. *Int J Adv Manuf Technol* 107:177–189
12. Scipioni SI, Lambiase F (2023) Yielding and post-yielding behavior of FDM parts under compression stress. *Int J Adv Manuf Technol* 128:1199–1211
13. Lambiase F, Scipioni SI, Paoletti A (2023) Mechanical characterization of FDM parts through instrumented flat indentation. *Int J Adv Manuf Technol* 125(9–10):4201–4211
14. Lambiase F, Scipioni SI, Paoletti A (2022) Determination of local density in components made by fused deposition modeling through indentation test. *Int J Adv Manuf Technol* 122(3–4):1467–1478
15. Gao X, Qi S, Kuang X, Su Y, Li J, Wang D (2021) Fused filament fabrication of polymer materials: a review of interlayer bond. *Addit. Manuf.* 37:101658
16. Aliheidari N, Tripuraneni R, Ameli A, Nadinpalli S (2017) Fracture resistance measurement of fused deposition modeling 3D printed parts. *Polym Test* 60:94–101

17. Young D, Wetmore N, Czabaj M (2018) Interlayer fracture toughness of additively manufactured unreinforced and carbon-fiber-reinforced acrylonitrile butadiene styrene. *Addit. Manuf.* 22:508–515
18. Fonseca J, Ferreira IA, de Moura MFSF, Machado M, Alves JL (2019) Study of the interlaminar fracture under mode I loading on FFF printed parts. *Compos Struct* 214:316–324
19. Barile C, Casavola C, Cazzato A (2018) Acoustic emissions in 3D printed parts under mode I delamination test. *Materials* 11(9):1760
20. Khudiakova A, Arbeiter F, Spoerk M, Wolfahrt M, Godec D, Pinter G (2019) Inter-layer bonding characterisation between materials with different degrees of stiffness processed by fused filament fabrication. *Addit. Manuf.* 28:184–193
21. Marsavina L, Stoia DI, Emanoil L (2021) Fracture toughness in additive manufacturing by selective laser sintering: an overview. *Mater. Des. Process. Commun* 3(6):e254
22. Santos JD, Fernandez A, Lluís R, Blanco N (2022) Experimental characterization and analysis of the in-plane elastic properties and interlaminar fracture toughness of a 3D-printed continuous carbon fiber-reinforced composite. *Polymers* 14(3):506
23. Hart KR, Dunn RM, Sietins JM, Holfmeister Mock CM, Mackay ME, Wetzel ED (2018) Increased fracture toughness of additively manufactured amorphous thermoplastics via thermal annealing. *Polymer* 144:192–204
24. Rabbi MF, Chalivendra V (2021) Improvement in interfacial fracture toughness of multi-material additively manufactured composites through thermal annealing. *Forces Mech.* 5:100051
25. Spoerk M, Gonzalez-Gutierrez J, Sapkota J, Schuschnigg S, Holzer C (2018) Effect of the printing bed temperature on the adhesion of parts produced by fused filament fabrication. *Plastics, Rubber and Composites* 47(1):17–24
26. Harris M, Potgieter J, Archer R, Arif KM (2019) Effect of material and process specific factors on the strength of printed parts in fused filament fabrication: a review of recent developments. *Materials* 12(10):1664
27. Stamopoulos AG, Scipioni SI, Lambiase F (2023) Experimental characterization of the interlayer fracture toughness of FDM components. *Compos Struct* 320:117213
28. ASTM 5528/D5528-21. Standard test method for Mode I interlaminar fracture toughness of unidirectional fiber-reinforced polymer matrix composites
29. DIN EN 1465- 2019. Adhesives- determination of tensile lap-shear strength of bonded assemblies
30. Irwin GR, Kies J (1997) Critical energy rate analysis of fracture strength. *Spie Milestone Series MS 137*:136–141
31. Stratakis D (2017) Performance of aerospace composites in the presence of process-induced defects. MSc Thesis, Cranfield University.

**Publisher's note** Springer Nature remains neutral with regard to jurisdictional claims in published maps and institutional affiliations.